Designing High-Performance LED Phosphors by Controlling the Phase Stability via a Heterovalent Substitution Strategy

Chen Cheng, Lixin Ning,* Xiaoxing Ke, Maxim S. Molokeev, Zelin Wang, Guojun Zhou, Yu-Chun Chuang, and Zhiguo Xia*

Phosphor-converted white light-emitting diodes (LEDs) are currently playing key roles in the lighting and display industries and trigger urgent demands for the discovery of "good" phosphors with high quantum efficiency, improved thermal stability, and controllable excitation/emission properties. Herein, a general and efficient heterovalent substitution strategy is demonstrated in $K_2HfSi_3O_9:Eu^{2+}$ achieved by Ln^{3+} (Ln = Gd, Tb, Dy, Tm, Yb, and Lu) doping to optimize luminescence properties, and as an example, the Lu^{3+} substitution leads to improvement of emission intensity and thermal stability, as well as tunable emission color from blue to cyan. The structural stability and Eu^{2+} occupation via Lu^{3+} doping have been revealed by the structural elaboration and density functional theory calculations, respectively. It is shown that heterovalent substitution allows predictive control of site preference of luminescent centers and therefore provides a new method to optimize the solid-state phosphors for LEDs.

1. Introduction

Nowadays, energy-efficient phosphor-converted white light-emitting diodes (WLEDs) are widely considered as next-generation solid state lighting sources to replace traditional incandescent lamp or fluorescent lamp and also as backlights for liquid crystal displays (LCDs) applications.[1] The most typical approach to generating white light is by uniting a blue or UV (ultraviolet) LED chip and one or more phosphors that can be pumped by the excitation light source.[2] Therefore, it is important to exploit "good" phosphors for LEDs application which meet the application demands simultaneously: i) high photoluminescence (PL) quantum efficiency (QE) and emission intensity; ii) excellent thermal quenching (TQ) property especially for the high power condition or laser LEDs; and iii) controlled excitation/emission property to fulfill different application requirements including the full-spectrum lighting, special light source or display.[3] The most common approach to developing new phosphors is by selecting suitable inorganic matrices and doped activators.[4] However, this way is difficult because new inorganic hosts become rare and their luminescence properties are also hardly predictable. Recently, learning from a mineral structure to develop appropriate matrices for new phosphors as

C. Cheng, G. J. Zhou, Prof. Z. G. Xia
The Beijing Municipal Key Laboratory of New Energy Materials
and Technologies
School of Materials Sciences and Engineering
University of Science and Technology Beijing
Beijing 100083, P. R. China
E-mail: xiazg@ustb.edu.cn

Prof. L. X. Ning
Anhui Key Laboratory of Optoelectric Materials
Science and Technology
Key Laboratory of Functional Molecular Solids
Ministry of Education
Anhui Normal University
Wuhu, Anhui 241000, P. R. China
E-mail: ninglx@mail.ahnu.edu.cn

Prof. X. X. Ke, Z. L. Wang
Institute of Microstructure and Property of Advanced Materials
Beijing University of Technology
Beijing 100124, P. R. China

Prof. M. S. Molokeev
Laboratory of Crystal Physics
Kirensky Institute of Physics
Federal Research Center KSC SB RAS
Krasnoyarsk 660036, Russia

Prof. M. S. Molokeev
Department of Engineering Physics and Radioelectronics
Siberian Federal University
Krasnoyarsk 660041, Russia

Prof. M. S. Molokeev
Department of Physics
Far Eastern State Transport University
Khabarovsk 680021, Russia

Dr. Y.-C. Chuang
National Synchrotron Radiation Research Center
Hsinchu 300, Taiwan

Prof. Z. G. Xia
State Key Laboratory of Luminescent Materials and Devices
and Guangdong Provincial Key Laboratory of Fiber Laser Materials
and Applied Techniques
South China University of Technology
Guangzhou 510641, P. R. China
E-mail: xiazg@scut.edu.cn

proposed by our group becomes a useful way which has been effectively applied for materials discovery.[5] For example, several rare earth phosphors with an unprecedented ultranarrow emission band have been designed in UCr_4C_4-type mineral model.[6] Moreover, the proposed chemical unit co-substitution strategy in our group has been also adopted to optimize the luminescence properties of phosphors by modifying the chemical compositions and the local environments of activators.[7] In this context, new blue-emitting $K_2BaCa(PO_4)_2:Eu^{2+}$ phosphor with highly thermal stable luminescence has been discovered,[8] and the solid solution of $(CaMg)_x(NaSc)_{1-x}Si_2O_6$ has been revealed as a typical example for cations' co-substitution model leading to the appearance of the two spectroscopically independent emission bands.[9]

In terms of the currently used design principles in the discovery of new phosphors, there are limited efficient strategies to find high-performance "good" phosphors with high QE, improved thermal stability, and controllable emission colors. Thus, modification of local environments of activators, especially for the phosphors with multiple sites, by chemical substitutions becomes a possible and essential approach to optimizing luminescence properties. Accordingly, heterovalent substitutions in anionic and cationic positions of solid-state materials are an effective approach to changing the chemical compositions of the host and directly affecting the local structures of the activators. Herein, we demonstrate a remarkable and general heterovalent substitution strategy in $K_2HfSi_3O_9:Eu^{2+}$ to "kill three birds with one arrow" with high QE, improved thermal stability, and controllable emission properties as discussed below. $K_2HfSi_3O_9$ is derived from wadeite-type mineral model with high chemical flexibility for substitution, and several blue and green phosphors doped with Eu^{2+} in this family have been previously reported.[10] In this study, as a general way, Ln^{3+} (Ln = Gd, Tb, Dy, Tm, Yb, and Lu) ions have been successfully doped in $K_2HfSi_3O_9$, and the pure phase samples have been obtained even if the Ln^{3+} doping content reaches a relative high content of $x = 0.25$ to replace the designed Hf site. Moreover, such a heterovalent substitution allows predictive control of phase stability, local structure, and site preference of Eu^{2+} luminescence centers. As such, the excitation and emission spectra can be tuned by modifying activator distribution in the different local structures developed by different charge compensation mechanisms, and the efficiency and emission intensity can be increased owing to the improved chemical equilibrium to reduce Eu^{3+} to Eu^{2+}. Finally, the thermal stability can be also enhanced due to the formation of single thermal-stable luminescent centers. This study paves a way for the exploration of site engineering originated from the heterovalent substitution and the development of new phosphors with optimized luminescence properties.

2. Result and Discussion

$K_2HfSi_3O_9$ possess the same structure as $K_2ZrSi_3O_9$ (ICSD-56898), which belongs to wadeite-type silicates.[10b,11] **Figure 1**a demonstrates the typical wadeite layered structure of $K_2HfSi_3O_9$ (abbreviated as KHSO hereafter). The framework is composed of $[Si_3O_9]^{6-}$ rings connected to isolated octahedrons $[HfO_6]^{8-}$,

and the rings are formed by three corner-linked $[SiO_4]^{4-}$ tetrahedrons distributed on different planes. The K atoms are each coordinated by nine oxygen atoms and are located in the interspace of the framework. As discussed previously, the wadeite-type compounds as represented by KHSO have a high crystal chemical flexibility and are tolerant for ionic substitutions. Herein, we first designed the targeted compounds with the chemical compositions of $K_2Hf_{0.95}Ln_{0.05}Si_3O_9:0.01Eu$ (Ln = Gd, Tb, Dy, Tm, Yb, and Lu) and prepared all the samples under the same experimental conditions. As shown in Figure 1b, all the samples possess the same phase as KHSO, indicating that the general heterovalent substitution strategy of Ln^{3+} at the designed Hf^{4+} sites, which have little effect on the crystal structure. In the following, we chose the substitution of Lu^{3+} for further discussion in view of its similar ionic size to that of Hf^{4+} and the associated interesting PL properties (see below). Figure 1c shows the powder X-ray diffraction (PXRD) pattern of $K_2Hf_{1-x}Lu_xSi_3O_9$ (abbreviated as KHL_xSO hereafter) (x = 0–0.25) samples, and all the patterns agree well with the standard file of KHSO. The dependence of unit cell volume (V) on Lu^{3+} concentration (x) of $KHL_xSO:\gamma Eu$ ($\gamma = 0$ and 0.05) obtained from PXRD patterns [Figure S1a, Supporting Information (SI)] are displayed in Figure S1b in the SI. For both $\gamma = 0$ and 0.05 series, the cell volumes increase with increasing Lu^{3+} content, and the increasing extent of the former series is a little more pronounced than the latter, showing a slight influence of Eu doping on the cell volume. Rietveld refinements of the synchrotron radiation X-ray diffraction (XRD) data for the two representative samples KHL_xSO (x = 0 and 0.2) were performed and the results are shown in Figure 1d,e, respectively. For KHSO, all peaks except for those of HfO_2 impurity phase (wt. ≈0.33%) were indexed to the hexagonal cell (P63/m) with parameters close to $K_2ZrSi_3O_9$, and $KHL_{0.2}SO$ displays the same structure as KHSO without any impurity. Furthermore, the refinement for $KHL_{0.2}SO$ reveals that dopants Lu^{3+} occupy not only Hf^{4+} sites but also K^+ sites, and the derived chemical formula can be written as $K_{1.922(1)}Lu_{0.078(1)}Hf_{0.92(2)}Lu_{0.08(1)}Si_3O_9$. The refined Lu^{3+} occupancy ratio at K^+ and Hf^{4+} sites deviates from the ideal value (1/2) required for charge balance $3Lu^{3+} \rightarrow K^+ + 2Hf^{4+}$. In such a case, the refinement results were stable and gave low R-factors. The calculated residual factor values were $R_p = 3.76\%$, and $R_{wp} = 5.22\%$ for KHSO; $R_p = 2.86\%$, and $R_{wp} = 3.96\%$ for $KHL_{0.2}SO$ (see details in Table S1, SI), and the coordinates of atoms and main bond lengths are listed in Table S2 in the SI.

To further study the KHSO phase before and after Lu^{3+} doping, the two phases were comparatively investigated by transmission electron microscopy (TEM). First, energy dispersive X-ray spectroscopy (EDX) mapping and spectroscopy analysis of $KHL_{0.2}SO$ sample was performed, confirming a successful doping of Lu and Eu in KHSO structure, where the dopant was evenly distributed in the structure (see details in Figure S2, SI). And then, the selected area electron diffraction (SAED) was performed for structural analysis. The SAED patterns of KHSO and $KHL_{0.2}SO$ were shown in **Figure 2**a,b, both along [100] zone axis. The corresponding electron pattern using proposed structures of KHSO and $KHL_{0.2}SO$ were then simulated as shown in Figure 2c,d. Comparing the simulated patterns, it can be seen that $002n + 1$ diffraction spots are absent in both structures, although 002 has higher intensity
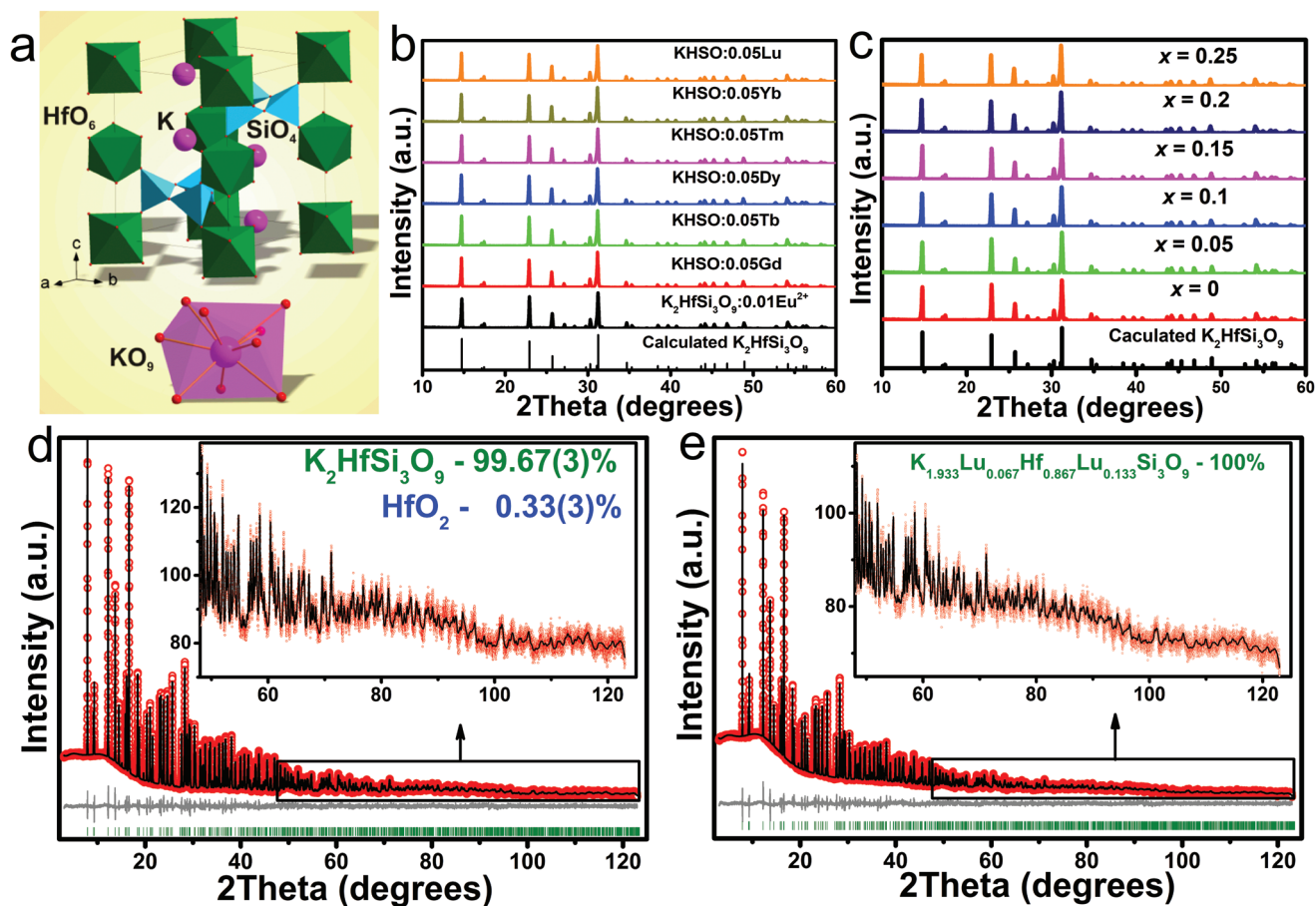
Figure 1. a) The unit cell structure of $K_2HfSi_3O_9$ with representative coordination polyhedra. b) XRD patterns of as-prepared $K_2Hf_{0.95}Ln_{0.05}Si_3O_9$:0.01Eu (Ln = Gd, Tb, Dy, Tm, Yb, and Lu) samples. c) PXRD patterns of KHL$_x$SO ($x = 0$–0.25). 25% Hf can be substituted by Lu without additional impurity phase. Rietveld refinements of the SXRD patterns of d) KHSO and e) KHL$_x$SO ($x = 0.2$); minor HfO_2 impurity appeared in KHSO and vanished in KHL$_x$SO ($x = 0.2$) also suggesting that the substituents Lu can stabilize the phase.

in doped structure due to the doping of Lu^{3+}. Comparing Figure 2a,c, it can be seen that the SAED pattern agree with the simulated pattern well, where $002n + 1$ diffraction spots are absent, and 002 has a rather low intensity. However, when comparing Figure 2b,d, it can be noticed that not only the 002 diffraction shows much higher intensity, the $002n + 1$ diffraction spots are clearly present. Considering the fact that Lu is doped in both sites of K and Hf, Lu is assumed to be at the sites of K and Hf in an ordered manner in the proposed model as a simplification, indicating a relatively high symmetry along c-axis. However, the presence of $002n + 1$ diffraction spots suggest that the doping of Lu in the K and Hf may be random and not follow an ordered replacement, and hence lower the symmetry along c-axis. On the other hand, the presence of $002n + 1$ diffraction spots is a strong evidence of the doping of Lu^{3+}. Moreover, we also captured an high resolution transmission electron microscopy (HRTEM) image of the KHSO structure, as shown in Figure 2e. The structure is viewed along [0–21] direction, and the corresponding crystallographic model is shown in Figure 2f. The position of Hf, K, and Si is indicated in both e,f), suggesting the consistent atoms occupations.

Figure 3a displays the emission spectra of KHL$_x$SO:γEu ($x = 0$, 0.2 and $\gamma = 0.01$, 0.05) measured under 365 nm excitation

at room temperature. The emissions are obviously attributed to $5d \rightarrow 4f$ transitions of dopants Eu^{2+}. For KHSO:0.01Eu, a broad emission band was observed, with the maximum at 464 nm and a tail on the long-wavelength side. The emission band can be deconvoluted into two Gaussian profiles peaking at around 464 and 496 nm (the inset). It suggests the presence of two types of Eu^{2+} centers (denoted as $Eu1^{2+}$ and $Eu2^{2+}$ centers, respectively).[10b] With increasing Eu^{2+} concentration from $\gamma = 0.01$ to 0.05, the 496 nm emission intensity is enhanced relative to that of the 464 nm emission, showing that the formation of $Eu2^{2+}$ centers is relatively favored. On the other hand, incorporation of Lu^{3+} in KHSO:0.01Eu leads to a remarkable increase of the 496 nm emission intensity and simultaneously the 464 nm emission becomes almost invisible. This indicates that the addition of Lu^{3+} in KHSO:0.01Eu promotes effectively the formation of $Eu2^{2+}$ centers at the cost of $Eu1^{2+}$ centers, and also the total number of Eu^{2+} centers. The same observation was made when Lu^{3+} concentration was varied in the range of $x = 0.05$–0.25 (Figure 3b).

Figure 3c gives the excitation spectra of KHL$_x$SO:0.01Eu for $x = 0$ and 0.2 monitored at 464 and 496 nm, respectively. The excitation onset of the 496 nm emission is redshifted by 28 nm with respect to that of the 464 nm emission, showing
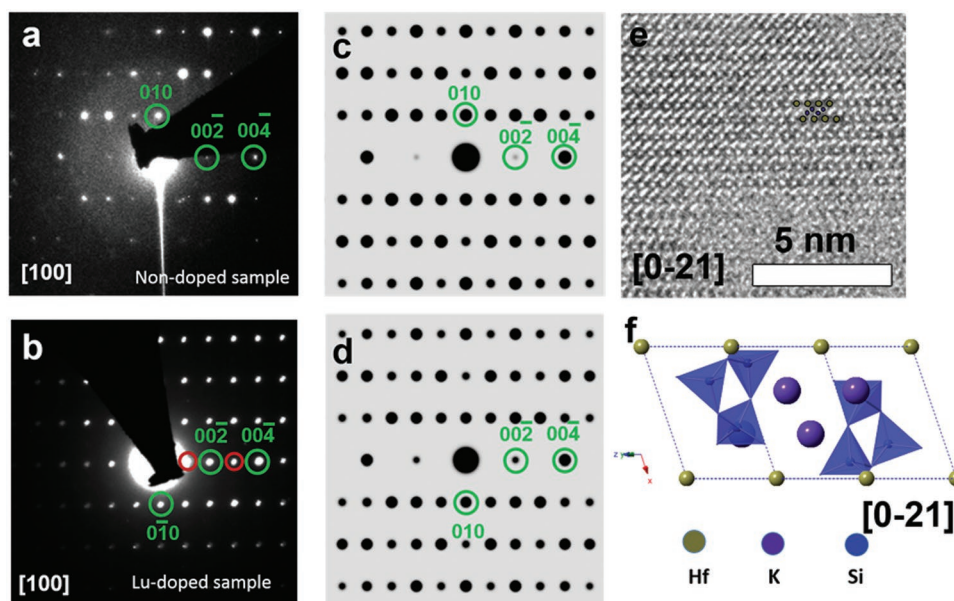
ADVANCED
SCIENCE NEWS
www.advancedsciencenews.com

ADVANCED
OPTICAL
MATERIALS
www.advopticalmat.de

Figure 2. SAED patterns of the a) KHSO sample and b) the Lu^{3+} doped $KHL_{0.2}SO$ sample acquired at [100] zone axis. c,d) The corresponding simulated electron diffraction pattern using proposed model of the KHSO and the $KHL_{0.2}SO$ samples. e) HRTEM image of the KHSO sample acquired at [0–21] zone axis. f) The corresponding crystallographic model of KHSO viewed along [0–21] zone axis.
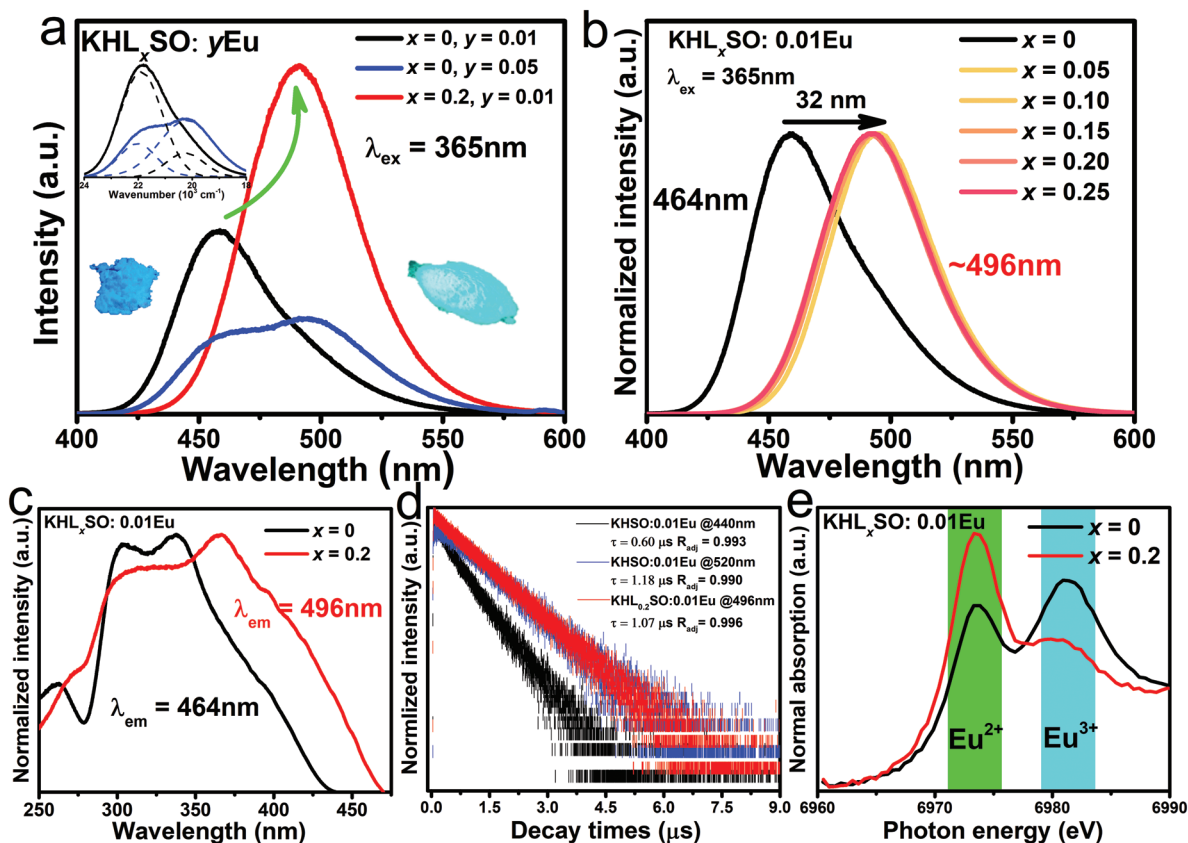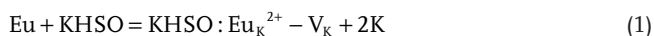

Figure 3. a) PL spectra of $KHL_xSO:yEu^{2+}$ ($x = 0$, 0.2 and $y = 0.01$, 0.05) showing that the emission peak redshifts from blue (464 nm) to blue-greenish (496 nm) with enhanced intensity upon increasing x. b) Normalized PL spectrum of $KHL_xSO:0.01Eu^{2+}$ with different Lu concentration ($x = 0$–0.25). c) Normalized PLE spectra of $KHL_xSO:0.01Eu^{2+}$ with $x = 0$ and 0.2. d) Luminescence decay curves of $KHL_xSO:0.01Eu^{2+}$ ($x = 0$ and 0.2) at different wavelengths. e) Normalized Eu L_3-edge XANES spectra of $KHL_xSO:0.01Eu$ ($x = 0$ and 0.2).

ADVANCED
SCIENCE NEWS
www.advancedsciencenews.com

ADVANCED
OPTICAL
MATERIALS
www.advopticalmat.de

again the presence of two types of Eu^{2+} centers with different local structures. Figure 3d shows that the decay curves of the 440 and 520 nm emissions of KHSO:0.01Eu can be well fitted by single exponential functions with derived lifetimes of 0.60 and 1.18 µs, respectively. Since these two emissions can be thought of originating mainly from $Eu1^{2+}$ and $Eu2^{2+}$ centers, respectively, the above decay behaviors stress the different local environments of the two centers. Moreover, the decay curve of the 496 nm emission from $KHL_{0.2}SO$:0.01Eu was also measured, and can be fitted by a single exponential function with a lifetime of 1.08 µs. This value is close to that of the 520 nm emission from KHSO:0.01Eu, confirming that both emissions arise from the same $Eu2^{2+}$ centers.
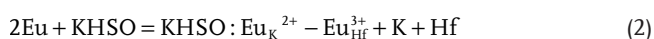
Figure 3e depicts the normalized Eu-L_3 edge X-ray absorption near-edge structure (XANES) spectra of KHL_xSO:0.01Eu ($x = 0$ and 0.2). The two peaks at about 6975 and 6982 eV are due to the $2p_{3/2} \rightarrow 5d$ transitions of Eu^{2+} and Eu^{3+}, respectively,[7] and the peak area is proportional to the number of ions. The results indicate the positive role of Lu^{3+} incorporation in increasing the number of Eu^{2+} relative that of Eu^{3+}, in line with the observation of increased Eu^{2+} emission intensity upon Lu^{3+} addition (Figure 3a). In fact, the quantum yield is increased from 85.7% (for KHSO:0.01Eu) to nearly 100% (for $KHL_{0.2}SO$:0.01Eu). Finally, the emission and excitation spectra of KHSO:0.01Eu co-doped with other Ln^{3+} ions (Ln = Gd, Tb, Dy, Tm, Yb) are presented in Figure S3 in the SI. A comparison of the spectra with those from KHSO:0.01Eu and KHLSO:0.01Eu indicates that the incorporation of these other Ln^{3+} ions exerts similar effect on the variation of the emission and excitation spectra, albeit not so pronounced as Lu^{3+}.

The PL measurements show that, in $KHSO:Eu^{2+}$, two kinds of Eu^{2+} centers with different local structures are present with comparable numbers. $Eu1^{2+}$ centers are responsible for the 464 nm emission and $Eu2^{2+}$ centers for the 496 nm emission. Since there is only one crystallographic site for either K^+ or Hf^{4+} in the host, one would intuitively assume that $Eu1^{2+}$ and $Eu2^{2+}$ centers are due to Eu^{2+} located at the two cation sites. However, Hf^{4+} is coordinated by six oxygen atoms with the Hf−O bond lengths all around 2.106 Å, and Eu^{2+} substitution at such a small site, if existed, would give an emission in the red spectral region.[12] As such, we speculate that the two centers are both due to Eu^{2+} located at K^+ sites but with different local structures possibly as a result of different charge compensation mechanisms.

To clarify this point, Eu^{2+} site occupations in KHSO were first investigated with density functional theory (DFT) calculations. Keeping in mind that trivalent Eu^{3+} co-exists with divalent Eu^{2+} in KHSO:Eu (Figure 3e), three types of charge-neutral defect complexes, $Eu_K^{2+}-V_K$, $Eu_K^{2+}-Eu_{Hf}^{3+}$, and $Eu_K^{3+}-Eu_{Hf}^{2+}$ were considered. DFT calculations revealed that the last type $Eu_K^{3+}-Eu_{Hf}^{2+}$ complexes are electronically unstable with respect to the second type $Eu_K^{2+}-Eu_{Hf}^{3+}$ and thus are discarded in the following discussion. The scenarios for $Eu_K^{2+}-V_K$ and $Eu_K^{2+}-Eu_{Hf}^{3+}$ substitutions can be expressed as:

$$Eu + KHSO = KHSO : Eu_K^{2+} - V_K + 2K \quad (1)$$

and

$$2Eu + KHSO = KHSO : Eu_K^{2+} - Eu_{Hf}^{3+} + K + Hf \quad (2)$$

The corresponding defect formation energies were calculated by

$$E_f = E(doped) - E(undoped) + 2\mu_K - \mu_{Eu} \quad (3)$$

and

$$E_f = E(doped) - E(undoped) + \mu_K + \mu_{Hf} - 2\mu_{Eu} \quad (4)$$

where $E(doped)$ and $E(undoped)$ represent the DFT total energies of the undoped and doped systems. µ is the atomic chemical potential of K, Hf, or Eu and was approximated by the energy of the corresponding metallic atom in view of the reducing atmosphere employed during material synthesis.

All symmetrically distinct $Eu_K^{2+}-V_K$ and $Eu_K^{2+}-Eu_{Hf}^{3+}$ configurations within a $2 \times 2 \times 1$ supercell were taken into account, including 15 $Eu_K^{2+}-V_K$ and 8 $Eu_K^{2+}-Eu_{Hf}^{3+}$. For them, the defect formation energies per Eu are predicted to be in the ranges of 0.616–0.946 and 0.920–1.379 eV, respectively. The relative preference for each independent substitution was further quantified by evaluating the occurrence probability, $P_k = \frac{1}{z_{tot}} \Omega_k \exp\left(-\frac{E_k}{kT}\right)$, (k = 1, ..., 23), where z_{tot} is the partition function, Ω_k is the multiplicity, E_k is the defect formation energy, k is the Boltzmann constant, and T (= 1773 K) is the synthesis temperature of the material. By summing the values of P_k for each kind of configurations, we found that the formation of $Eu_K^{2+}-V_K$ is much more favorable than $Eu_K^{2+}-Eu_{Hf}^{3+}$, with the overall probabilities being 0.892 and 0.108, respectively. Thus, Eu^{2+} location at the K^+ site with charge compensation by a V_K is much more thermodynamically stable than the same site location with charge compensation by an Eu_{Hf}^{3+}.

During the material synthesis, excess K_2CO_3 reagents were added in order to suppress the formation of the impurity phase. It is expected that the occurrence probability of charge compensation by a V_K would thus be reduced, which would conversely enhance the probability of the charge compensation by Eu_{Hf}^{3+}. Hence, the relative probability of $Eu_K^{2+}-Eu_{Hf}^{3+}$ complexes could be higher than that predicted thermodynamically, and would further increase with increasing Eu concentration due to more availability of Eu^{3+}. On the basis of these theoretical considerations and also the comparison of the theoretical analysis with experimental observations in Figure 3a, we can tentatively identify both $Eu1^{2+}$ (λ_{em} = 464 nm) and $Eu2^{2+}$ (λ_{em} = 496 nm) centers as Eu^{2+} located at K^+ sites but with different charge compensations by V_K and Eu_{Hf}^{3+}, respectively, as further substantiated below.

In KHSO, the K site (C_3 symmetry) is coordinated by nine oxygens within a distance of 3.3 Å, with the calculated (experimentally) K–O distances being 2.868 (2.843), 3.160 (3.126), and 3.254 (3.232) Å. Since the ionic radius of Eu^{2+} is smaller than that of K^+ by 0.21–0.26 Å in the same fold of coordination,[13] the Eu_K^{2+} substitution will lead to an inward relaxation of the coordination polyhedron. From the calculated defect formation energies, the most stable $Eu_K^{2+}-V_K$ and $Eu_K^{2+}-Eu_{Hf}^{3+}$ substitutions within each kind of configurations are distinguished by the unrelaxed long K–K distance of 8.172 Å and short K–Hf distance of 3.806 Å. Their optimized local structures show that both Eu_K^{2+} substitutions induce an inward shift (by 0.186–0.646 Å) of the nearest-neighbor

ADVANCED
SCIENCE NEWS
www.advancedsciencenews.com

ADVANCED
OPTICAL
MATERIALS
www.advopticalmat.de

six oxygens, and an outward shift of the farthest three oxygens up to Eu–O distances larger than 3.60 Å due to steric effects. Thus, virtually Eu_K^{2+} is coordinated by six oxygens and the corresponding local structures are displayed in **Figure 4**, along with that of K^+ for comparison. It shows that the local structural relaxation for $Eu_K^{2+}–V_K$ is isotropic with the average $Eu^{2+}–O^{2-}$ distance of 2.637 Å and the C_3 site symmetry is preserved (Figure 4b), whereas, for $Eu_K^{2+}–Eu_{Hf}^{3+}$, the relaxation is anisotropic with the average $Eu^{2+}–O^{2-}$ distance of 2.627 Å and no local symmetry is found (Figure 4c). The extent of distortions in the two cases may be characterized by the distortion index defined by [14]

$$D = \frac{1}{6} \sum_{i=1}^{6} \frac{|d_i - d_{av}|}{d_{av}} \qquad (5)$$

where d_i is the distance from Eu to the ith coordinating oxygen and d_{av} is the average distance. It is found that the D values for the most stable $Eu_K^{2+}–V_K$ and $Eu_K^{2+}–Eu_{Hf}^{3+}$ substitutions are 0.004 and 0.302, respectively. Besides for the most stable substations, DFT calculations also show that the D-values (0.005–0.025) for other $Eu_K^{2+}–V_K$ substitutions are generally smaller than those (0.018–0.033) for other $Eu_K^{2+}–Eu_{Hf}^{3+}$ substitutions. Given the similar d_{av} values, a larger distortion of the latter type of substitutions would lead to a larger crystal field splitting of the Eu^{2+} 5d levels, and hence a lower position of the lowest-energy 5d level with respect to the ground-state $Eu^{2+}(4f^7)$ level.[15] These results indicate the onset of $4f{\to}5d$ excitation/

absorption spectrum for $Eu_K^{2+}–Eu_{Hf}^{3+}$ is lower in energy than that for $Eu_K^{2+}–V_K$. Therefore, the 496 and 464 nm emissions and the corresponding excitation spectra can be assigned as Eu_K^{2+} centers with Eu_{Hf}^{3+} and V_K charge compensations, respectively.

Upon Lu^{3+} incorporation in KHSO, another type of charge compensation mechanism may be present, i.e., $Eu_K^{2+}–Lu_{Hf}^{3+}$. The substitution scenario is
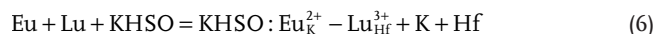
$$Eu + Lu + KHSO = KHSO : Eu_K^{2+} - Lu_{Hf}^{3+} + K + Hf \qquad (6)$$

and the corresponding defect formation energies were calculated by

$$E_f = E(doped) - E(undoped) + \mu_K + \mu_{Hf} - \mu_{Eu} - \mu_{Lu} \qquad (7)$$

Similar to $Eu_K^{2+}–Eu_{Hf}^{3+}$, there are eight symmetrically distinct $Eu_K^{2+}–Lu_{Hf}^{3+}$ substitutions within the supercell. By contrast, however, the calculated defect formation energies for this type of substitutions are now negative, ranging from −0.959 to −0.526 eV. This is a striking result, indicating that $Eu_K^{2+}–Lu_{Hf}^{3+}$ are not only much more energetically favorable than $Eu_K^{2+}–V_K$ and $Eu_K^{2+}–Eu_{Hf}^{3+}$, but also are thermodynamically stable. That is, the incorporation of Lu^{3+} dramatically reduces the energy cost to substitute an Eu^{2+} at the K^+ site, and can lead to a significant increase of Eu_K^{2+} concentration. In addition, for the optimized local structures, the average $Eu^{2+}–O^{2-}$ bond length is 2.661 Å and the distortion indexes are $D = 0.013–0.029$, both close to the values for $Eu_K^{2+}–Eu_{Hf}^{3+}$. A comparison of the local structures for the most stable $Eu_K^{2+}–Lu_{Hf}^{3+}$ and $Eu_K^{2+}–Eu_{Hf}^{3+}$ substitutions is shown in Figure 4c,d, and the clear similarity between them implies similar spectral regions in which Eu^{2+} 4f–5d emission/excitation spectra are located.

On the basis of above theoretical results, the experimentally observed PL properties before and after Lu^{3+} incorporation can be explained as follows. In KHSO:Eu^{2+}, Eu^{2+} substitution at the K^+ site can in principle be charge compensated by a V_K or an Eu_{Hf}^{3+}. Although the former charge compensation is thermodynamically more stable that the latter, the excess use of K^+ during material synthesis makes easier the formation of the latter as compared to the former. Thus, both types of charge compensations, $Eu_K^{2+}–V_K$ and $Eu_K^{2+}–Eu_{Hf}^{3+}$, are present in KHSO:Eu^{2+}, giving rise to the 464 and 496 nm emissions, respectively. When Lu^{3+} is incorporated in KHSO:Eu^{2+}, the Lu_{Hf}^{3+} substation is much more preferred than Eu_{Hf}^{3+} due to the much closer ionic radii between Lu^{3+} and Hf^{4+} than between Eu^{3+} and Hf^{4+}, which renders $Eu_K^{2+}–Lu_{Hf}^{3+}$ substitutions dominant in KHLSO:Eu^{2+} and consequently observation of a single emission band around 496 nm. Moreover, the thermodynamic stability of $Eu_K^{2+}–Lu_{Hf}^{3+}$ in
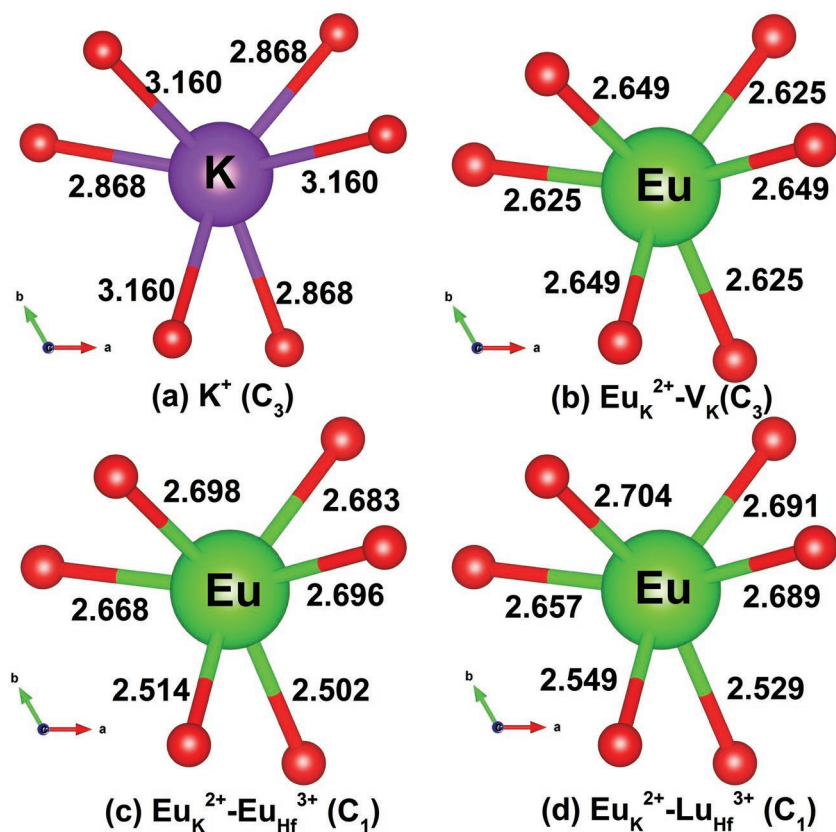

Figure 4. Optimized local structures of a) K^+ in KHSO, b,c) Eu^{2+} in KHSO and d) in KHLSO. The values of the bond lengths (in Å) and the site symmetries are indicated.
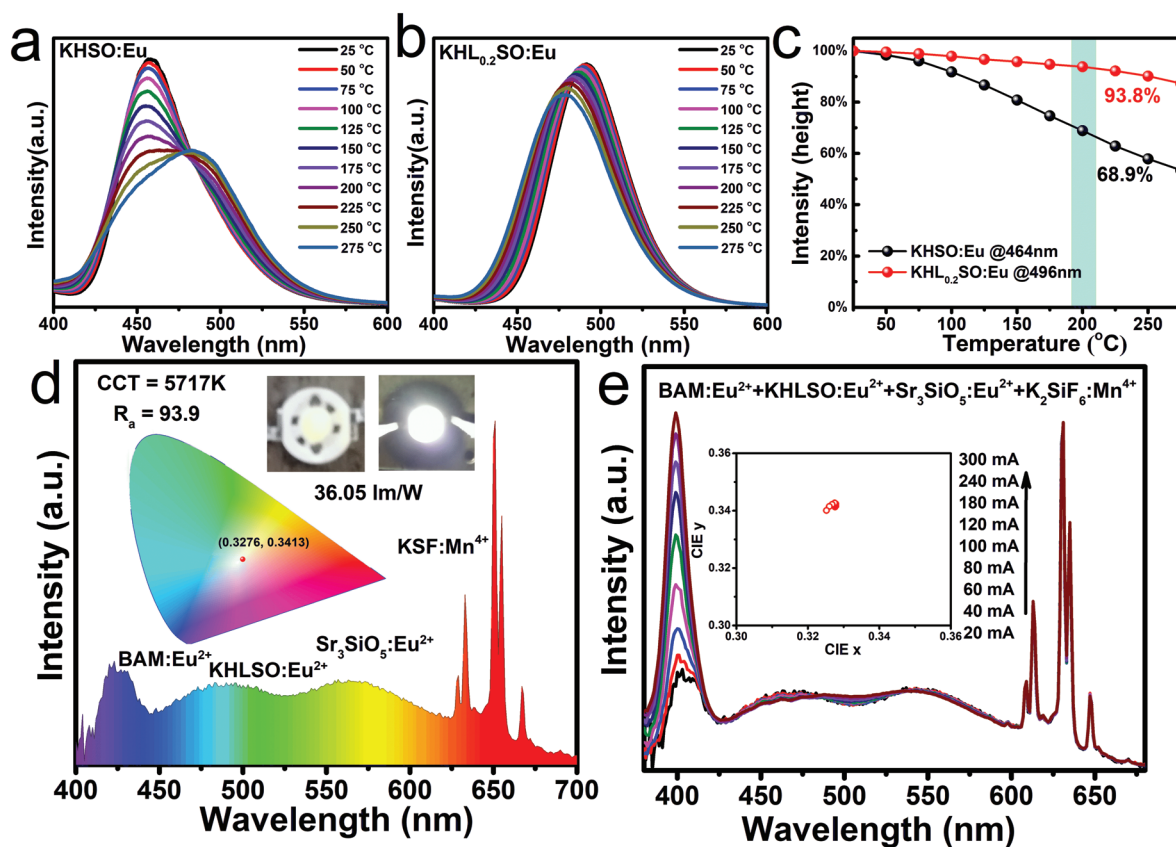
Figure 5. Thermal stability of $K_2HfSi_3O_9$:Eu and Lu-doped $K_2HfSi_3O_9$:Eu and the performance of fabricated WLEDs. Temperature-dependent Eu^{2+} emission spectra of a) KHSO: 0.01Eu and b) $KHL_{0.2}SO$:0.01Eu. c) Temperature dependence of the highest PL intensity of KHSO:0.01Eu and $KHL_{0.2}SO$:0.01Eu. d) PL spectrum and photos of the WLED device fabricated with the commercial blue phosphor BAM:Eu^{2+}, the present cyan phosphor $KHL_{0.2}SO$:Eu^{2+}, the commercial yellow phosphor Sr_3SiO_5:Eu^{2+}, the red phosphor K_2SiF_6:Mn^{4+}, and a UV chip. e) PL spectra and CIE chromaticity coordinates of the fabricated WLED under various forward bias currents.

KHLSO:Eu^{2+} will also result in a larger number of Eu^{2+} versus Eu^{3+} than in KHSO:Eu^{2+} at a fixed Eu doping concentration, in consistence with the XANES spectra (Figure 3e and Figure S4, SI). Finally, along this line of reasoning, co-doping KHSO:Eu^{2+} with other trivalent lanthanide ions (Ln^{3+}) with ionic radius smaller than Eu^{3+} could also produce similar effects on Eu^{2+} luminescence properties in KHSO:Eu^{2+}, as indeed observed in experiments (Figure S3, SI).

The TQ properties of Eu^{2+} luminescence have been investigated to evaluate the potential high power LEDs application of the phosphors. Temperature-dependent emission spectra measured from room temperature to 275 °C are displayed in **Figure 5**. It shows that, for KHSO:0.01Eu, the 464 nm emission intensity decreases much more rapidly than the 496 nm emission intensity with increasing temperature (Figure 5a). The high thermal stability of the 496 nm emission is further manifested by its temperature dependence measured for $KHL_{0.2}SO$:0.01Eu (Figure 5b). The intensity of this emission at 200 °C drops to 93.8% of the initial intensity at room temperature, whereas, for the 464 nm emission of KHSO:0.01Eu, only 68.9% of the initial intensity is kept (Figure 5c). The higher thermal stability of the 496 nm emission than the 464 nm emission can be understood in terms of the energy difference (ΔE_{5d}) between the emitting

5d level and the bottom of the host conduction band. First, the 496 and 464 nm emission were both attributed to Eu^{2+} located at K^+ sites but with $Lu_{Hf}^{3+}/Eu_{Hf}^{3+}$ and V_K charge compensations, i.e., Eu2^{2+} and Eu1^{2+} centers, respectively. It is thus expected the energy positions (ΔE_{4f}) of $Eu^{2+}(4f^7)$ ground-state levels for the two centers are similar with respect to the top of the host valence band. Secondly, the 4f–5d energy difference (ΔE_{4f-5d}) between the $4f^7$ ground-state level and the emitting 5d level is smaller for Eu2^{2+} than that for Eu1^{2+}, as evident from spectral properties and above crystal field analysis. Finally, according to $\Delta E_{5d} = E_{gap} - \Delta E_{4f} - \Delta E_{4f-5d}$, where E_{gap} is the host bandgap and is assumed to be invariant upon Lu^{3+} incorporation, the value of ΔE_{5d} is anticipated to be larger for Eu2^{2+} than that for Eu1^{2+}, leading to a lower thermal ionization probability and thus a higher luminescence thermal stability at 490 nm.

On the basis of the excellent luminescence characteristics, a WLEDs lamp was fabricated from a commercial blue phosphor BAM:Eu^{2+}, the present cyan phosphor $KHL_{0.2}SO$:Eu^{2+}, the commercial yellow phosphor Sr_3SiO_5:Eu^{2+}, the red phosphor K_2SiF_6:Mn^{4+}, and a UV chip (395 nm). Figure 5d shows the luminescence spectra and photos of the LED lamp under a drive current of 20 mA and a drive voltage of 3 V. The correlated color temperature (CCT) of the WLED is 5717 K and the

corresponding color rendering index (R_a) is determined to be 93.9. To further evaluate the dependence of WLED performance on the drive current, the PL spectrum was recorded under drive currents between 20 and 300 mA (Figure 5e). All the emission spectra are similar in shape. The WLED displays only very small fluctuation in color (CIE coordinate) even at a high flux current of 300 mA. This results demonstrate that KHLSO:Eu^{2+} phosphor is suitable as a cyan light component for high R_a WLEDs.

3. Conclusion

In summary, we have developed a general heterovalent substitution strategy by doping trivalent lanthanide ions (Gd, Tb, Dy, Tm, Yb, and Lu) into K$_2$HfSi$_3$O$_9$:Eu^{2+} phosphors, and allowed predictive control of site preference of luminescence centers and phase stability. This enabled us to discover and optimize "good" LED phosphors with simultaneous enhancement of the luminescence efficiency, thermal stability, and tunable PL. This strategy has been illustrated by Lu^{3+} substitution at Hf^{4+} and K$^+$ sites of K$_2$HfSi$_3$O$_9$, leading to the phase formation of K$_{2-1/3x}$Lu$_{1/3x}$Hf$_{1-2/3x}$Lu$_{2/3x}$Si$_3$O$_9$. With the Lu^{3+} substitution, the local structures of Eu^{2+} changed with different charge compensation mechanisms, and the reduction of Eu^{3+} into Eu^{2+} was promoted simultaneously resulting in an enhancement of Eu^{2+} cyan emission intensity. Moreover, the improvement of the luminescence thermal stability was ascribed to an enlargement of the energy difference between the emitting 5d level and the bottom of the host conduction band. The fabricated White LED based on KHLSO:Eu phosphors showed a high R_a (93.9), indicating that they can be used as an ideal cyan phosphor for high-quality pc-WLEDs. This work demonstrates that heterovalent substitution is an effective approach for the exploration of phosphors with remarkable luminescence performance.

4. Experimental Section

Materials and Preparation: The designed chemical formulae are written as K$_2$Hf$_{1-x}$Ln$_x$Si$_3$O$_9$:γEu^{2+} (Ln = Gd, Tb, Dy, Tm, Yb, and Lu), and the samples were synthesized by the high temperature solid-state method. According to the given stoichiometric ratios, the mixtures of K$_2$CO$_3$ (A.R.), HfO$_2$ (A.R.), SiO$_2$ (A.R.), and different rare-earth oxides (99.99%) were weighed and ground in an agate mortar and transferred into an alumina crucible. A slight excess of K$_2$CO$_3$ (5% in w.t.%) was added because of its sublimation character. Then they were sintered under a reducing atmosphere (10%H$_2$/90%N$_2$) at 1500 °C for 8 h, and cooled naturally to room temperature and finely ground with a mortar for further characterization.

Characterization: PXRD measurements were performed on a D8 Advance diffractometer (Bruker Corporation, Germany) at 40 kV and 40 mA with Cu Kα radiation (λ = 1.5406 Å). Synchrotron X-ray powder diffraction (SXRD) measurements were performed at TPS 09A (Taiwan Photon Source) of the National Synchrotron Radiation Research Center with a calibrated wavelength of 0.82656 Å. During the measurement, the powder sample was packed into a glass capillary, and the 1D powder diffraction patterns were recorded using MYTHEN 24K detector with 30 s exposure time. Rietveld refinements were conducted using TOPAS 4.2. TEM was performed on FEI Titan G2 microscope equipped with an aberration corrector for probe forming lens and a Bruker SuperX detector for EDX, accelerated at 300 kV. The sample was prepared by crushing the powder in ethanol before being dropped on a lacey carbon

film supported Cu grid. The Eu L_3-edge XANES spectra was obtained on the 1W2B beam line of the Beijing Synchrotron Radiation Facility. The PL emission, photoluminescence excitation (PLE) spectra, and temperature-dependent emission spectra were measured by a Hitachi F-4640 fluorescence spectrophotometer. The decay curves were collected on the FLSP920 fluorescence spectrophotometer equipped with an nF900 flash lamp as the excitation source. The PL spectra, color-rendering index (Ra), and color temperature (CCT) of the fabricated WLEDs were collected by an integrating sphere spectroradiometer system (ATA-1000, Everfine). The external and internal QE were measured using the integrated sphere on FLS920 instrument, and white BaSO4 powder was used as a reference to measure the absorption. The external (η_0), internal (η_i) QEs, and absorption efficiency (α_{abs}) were calculated by using the following equations,[16]

$$\eta_0 = \frac{\varepsilon}{\delta} = \frac{\int L_S}{\int E_R}, \quad \eta_i = \frac{\varepsilon}{\alpha} = \frac{\int L_S}{\int E_R - \int E_S}, \quad \alpha_{abs} = \frac{\alpha}{\delta} = \frac{\int E_R - \int E_S}{\int E_R} \quad (8)$$

where ε is the number of photons emitted by the sample, δ is the number of total photons excited by the light source, and α is the number of photons absorbed by the sample. L_S is the luminescence emission spectrum of the sample; E_R is the spectrum of the excitation light with BaSO$_4$ in the sphere; E_S is the spectrum of the excitation light with the sample in the sphere; and all the spectra were collected using the sphere.

5. Computational Methodology

The host K$_2$HfSi$_3$O$_9$ crystal was modeled by a 2 × 2 × 1 supercell, containing 16 K, 8 Hf, 24 Si, and 72 O atoms. One Eu^{2+} or Eu^{3+} was substituted at a K site with excess charge compensated by a V$_K$, Eu$_{Hf}$$^{3+}$, Lu$_{Hf}$$^{3+}$, or Eu$_{Hf}$$^{2+}$. Periodic DFT calculations were carried out using PBE+U approach with U = 2.5 eV for Eu 4f electrons,[17] as implemented in the Vienna Ab-initio simulation package (VASP).[18] The K(3$p^6$4s^1), Hf(5$s^2$4$p^6$6$s^2$5d^2), Si(3$s^2$3p^2), O(2$s^2$2p^4), Lu(5$p^6$6$s^2$5d^1), and Eu(5$s^2$5$p^6$4$f^7$6s^2) were treated as valence electrons, and their interactions with the respective cores were described by the projected augmented wave approach.[19] The atomic structures were fully optimized until the total energies and the forces on the atoms were converged to 10^{-6} eV and 0.01 eV Å^{-1}, respectively. One k-point Γ employed was used to sample the Brillouin zone, and the cut-off energy of the plane-wave basis was set to 530 eV. Calculations for the metallic K, Hf, Lu, and Eu (two-atom cell) were performed with the same convergence criteria as that for the bulk materials and a 16 × 16 × 16 k-point grid.

Supporting Information

Supporting Information is available from the Wiley Online Library or from the author.

Conflict of Interest

The authors declare no conflict of interest.

[1] a) E. F. Schubert, J. K. Kim, *Science* **2005**, *308*, 1274. b) Z. Xia, Q. Liu, *Prog. Mater. Sci.* **2016**, *84*, 59. c) L. Wang, R. J. Xie, T. Suehiro, T. Takeda, N. Hirosaki, *Chem. Rev.* **2018**, *118*, 1951.

[2] a) P. Pust, P. J. Schmidt, W. Schnick, *Nat. Mater.* **2015**, *14*, 454. b) H. Terraschke, C. Wickleder, *Chem. Rev.* **2015**, *115*, 11352.

[3] a) M. Zhao, Z. Xia, X. Huang, L. Ning, R. Gautier, M. S. Molokeev, Y. Zhou, Y.-C. Chuang, Q. Zhang, Q. Liu, *Sci. Adv.* **2019**, *5*, eaav0363. b) S. Li, L. Wang, D. Tang, Y. Cho, X. Liu, X. Zhou, L. Lu, L. Zhang, T. Takeda, N. Hirosaki, R.-J. Xie, *Chem. Mater.* **2018**, *30*, 494. c) Y. H. Kim, P. Arunkumar, B. Y. Kim, S. Unithrattil, E. Kim, S. H. Moon, J. Y. Hyun, K. H. Kim, D. Lee, J. S. Lee, W. B. Im, *Nat. Mater.* **2017**, *16*, 543.

[4] Z. Wang, J. Ha, Y. H. Kim, W. B. Im, J. McKittrick, S. P. Ong, *Joule* **2018**, *2*, 914.

[5] Z. Xia, Z. Xu, M. Chen, Q. Liu, *Dalton Trans.* **2016**, *45*, 11214.

[6] a) P. Pust, V. Weiler, C. Hecht, A. Tucks, A. S. Wochnik, A. K. Henss, D. Wiechert, C. Scheu, P. J. Schmidt, W. Schnick, *Nat. Mater.* **2014**, *13*, 891. b) M. Zhao, H. Liao, L. Ning, Q. Zhang, Q. Liu, Z. Xia, *Adv. Mater.* **2018**, *30*, 1802489. c) H. Liao, M. Zhao, M. S. Molokeev, Q. Liu, Z. Xia, *Angew. Chem., Int. Ed.* **2018**, *57*, 11728.

[7] a) M. Chen, Z. Xia, M. S. Molokeev, T. Wang, Q. Liu, *Chem. Mater.* **2017**, *29*, 1430. b) L. Wang, R. J. Xie, Y. Li, X. Wang, C. G. Ma, D. Luo, T. Takeda, Y. T. Tsai, R. S. Liu, N. Hirosaki, *Light: Sci. Appl.* **2016**, *5*, e16155.

[8] J. Qiao, L. Ning, M. S. Molokeev, Y. C. Chuang, Q. Liu, Z. Xia, *J. Am. Chem. Soc.* **2018**, *140*, 9730.

[9] Z. Xia, G. Liu, J. Wen, Z. Mei, M. Balasubramanian, M. S. Molokeev, L. Peng, L. Gu, D. J. Miller, Q. Liu, K. R. Poeppelmeier, *J. Am. Chem. Soc.* **2016**, *138*, 1158.

[10] a) X. Ding, G. Zhu, W. Geng, M. Mikami, Y. Wang, *J. Mater. Chem. C* **2015**, *3*, 6676. b) Z. Tang, G. Zhang, Y. Wang, *ACS Photonics* **2018**, *5*, 3801.

[11] H. Xu, A. Navrotsky, M. L. Balmer, Y. Su, *Phys. Chem. Miner.* **2005**, *32*, 426.

[12] J. Qiao, L. Ning, M. S. Molokeev, Y. C. Chuang, Q. Zhang, K. R. Poeppelmeier, Z. Xia, *Angew. Chem., Int. Ed.* **2019**, *131*, 11645.

[13] R. D. Shannon, *Acta Crystallogr. A* **1976**, *32*, 751.

[14] W. Baur, *Acta Crystallogr., Sect. B: Struct. Crystallogr. Cryst. Chem.* **1974**, *30*, 1195.

[15] P. Dorenbos, *J. Phys.: Condens. Matter* **2003**, *15*, 4797.

[16] a) K. Ohkubo, T. Shigeta, *J. Illuminat. Eng. Inst. Japan* **1999**, *83*, 87; b) L. Wang, X. Wang, T. Kohsei, K. Yoshimura, M. Izumi, N. Hirosaki, R. J. Xie, *Opt. Express* **2015**, *23*, 28707.

[17] a) S. Dudarev, G. Botton, S. Savrasov, C. Humphreys, A. Sutton, *Phys. Rev. B* **1998**, *57*, 1505. b) A. Chaudhry, R. Boutchko, S. Chourou, G. Zhang, N. Grønbech-Jensen, A. Canning, *Phys. Rev. B* **2014**, *89*, 155105.

[18] a) G. Kresse, J. Furthmüller, *Phys. Rev. B* **1996**, *54*, 11169. b) G. Kresse, D. Joubert, *Phys. Rev. B* **1999**, *59*, 1758.

[19] P. E. Blochl, *Phys. Rev. B* **1994**, *50*, 17953.